

Temperature and polarization CMB maps from primordial non-Gaussianities of the local type

Michele Liguori¹, Amit Yadav², Frode K. Hansen³, Eiichiro Komatsu⁴, Sabino Matarrese⁵, Benjamin Wandelt²

¹*Department of Applied Mathematics and Theoretical Physics,
Centre for Mathematical Sciences, University of Cambridge,
Wilberforce Road, Cambridge, CB3 0WA, United Kingdom*

²*Department of Astronomy, University of Illinois at Urbana-Champaign, 1002 W. Green Street, Urbana, IL 61801*

³*Institute of Theoretical Astrophysics, University of Oslo, P.O. Box 1029 Blindern, 0315 Oslo, Norway*

⁴*Department of Astronomy, University of Texas at Austin, 2511 Speedway, RLM 15.30 6, TX 78712 and*

⁵*Dipartimento di Fisica “G. Galilei”, Università di Padova and INFN,
Sezione di Padova, via Marzolo 8, I-35131, Padova, Italy*

(Dated: June 23, 2021)

The forthcoming *Planck* experiment will provide high sensitivity polarization measurements that will allow us to further tighten the f_{NL} bounds from the temperature data. Monte Carlo simulations of non-Gaussian CMB maps have been used as a fundamental tool to characterize non-Gaussian signatures in the data, as they allow us to calibrate any statistical estimators and understand the effect of systematics, foregrounds and other contaminants. We describe an algorithm to generate high-angular resolution simulations of non-Gaussian CMB maps in temperature and polarization. We consider non-Gaussianities of the local type, for which the level of non-Gaussianity is defined by the dimensionless parameter, f_{NL} . We then apply the temperature and polarization fast cubic statistics recently developed by Yadav *et al.* to a set of non-Gaussian temperature and polarization simulations. We compare our results to theoretical expectations based on a Fisher matrix analysis, test the unbiasedness of the estimator, and study the dependence of the error bars on f_{NL} . All our results are in very good agreement with theoretical predictions, thus confirming the reliability of both the simulation algorithm and the fast cubic temperature and polarization estimator.

I. INTRODUCTION

Small, but non-vanishing non-Gaussianity of primordial cosmological perturbations is a general prediction of inflation. The amplitude of the expected non-Gaussian signal is model-dependent and can vary by many orders of magnitude from one inflationary scenario to another. For example, the non-Gaussian signatures produced by single-field slow-roll inflation models are tiny and far below the present and forthcoming experimental sensitivity [1, 2]. On the other hand many other scenarios predict a level of non-Gaussianity that is within reach of present and forthcoming experiments like WMAP and *Planck* (see e.g. [3, 4, 5, 6, 7, 8, 9, 10]). For this reason an experimental detection of non-Gaussianity would rule out the simplest scenarios of slow-roll inflation. More in general, experimental bounds on primordial non-Gaussianity allow us to significantly constrain different scenarios for the generation of perturbations in the context of primordial inflation.

Primordial non-Gaussianity from inflation can be described in terms of the 3-point correlation function of the curvature perturbations, $\Phi(\mathbf{k})$, in Fourier space:

$$\langle \Phi(\mathbf{k}_1)\Phi(\mathbf{k}_2)\Phi(\mathbf{k}_3) \rangle = (2\pi)^3 \delta^{(3)}(\mathbf{k}_1 + \mathbf{k}_2 + \mathbf{k}_3) F(k_1, k_2, k_3) . \quad (1)$$

Note that Φ is the curvature perturbation during the matter era, and temperature anisotropy in the Sachs-Wolfe limit is given by $\Delta T/T = -\Phi/3$. Depending on the shape of the function $F(k_1, k_2, k_3)$, we can divide non-Gaussianity from inflation into two different classes: local non-Gaussianity, where F is large for *squeezed* configurations (i.e. configurations in which $k_1 \ll k_2, k_3$), and non-local non-Gaussianity of the *equilateral* type, where the largest contributions come from modes with $k_1 \sim k_2 \sim k_3$. The former kind of non-Gaussianity can be produced in models where primordial perturbations are not generated by inflaton itself but by a second light scalar field (like e.g. in the curvaton model). The latter comes from single field models with a non-minimal Lagrangian containing higher derivative operators. In this paper we will focus on non-Gaussianity of the local type, where the primordial curvature perturbation Φ can be described in terms of the following real space parameterization:

$$\Phi(\mathbf{x}) = \Phi_L(\mathbf{x}) + f_{\text{NL}} (\Phi_L^2(\mathbf{x}) - \langle \Phi_L^2(\mathbf{x}) \rangle) . \quad (2)$$

In the last formula f_{NL} is a parameter that defines the amplitude of the primordial non-Gaussian signal. Our previous statement about the detectability of non-Gaussian signatures from inflation can be precisely quantified in terms of this parameter. In standard scenarios of single-field slow roll inflation f_{NL} is generally predicted to be very small and undetectable ($\sim 10^{-2}$ at the end of inflation, ~ 1 when second order perturbation theory after inflation is taken into account) whereas other scenarios, like the curvaton or variable decay width models, can naturally give rise to relatively large values of f_{NL} ($f_{\text{NL}} \sim 10$). This justifies the claim that an experimental detection of f_{NL} would rule out the simplest single-field inflationary paradigm and allow us to put significant constraints on the other inflationary scenarios.

The best way to put experimental bounds on f_{NL} is to look for non-Gaussianities in CMB anisotropies (but it has been recently pointed out that future deep galaxy-surveys and 21 cm background measurements could provide promising results [11, 12, 13]). The most stringent constraints on f_{NL} so far come from measurements of the CMB angular bispectrum on the WMAP temperature data $-36 < f_{\text{NL}} < 100$ (95% *c.l.*) [14, 15, 16]. This constraint corresponds to a $1 - \sigma$ error of $\Delta f_{\text{NL}} = 34$. A Fisher matrix analysis by the authors of [17] showed that WMAP will in principle be able to reach $\Delta f_{\text{NL}} = 20$, while the forthcoming *Planck* satellite can achieve $\Delta f_{\text{NL}} = 5$. This means that *Planck* will be sensitive to the level of non-Gaussianity predicted by a vast range of different inflationary models. We can improve this constraint further by including the polarization data. For WMAP all the non-Gaussian information is basically contained in the temperature data, due to large errors in polarization measurements. *Planck*, on the other hand, will characterize polarization fluctuations with high accuracy. This will allow us to exploit the additional information contained in polarization data and to gain a further factor of order 2 in Δf_{NL} , thus yielding $\Delta f_{\text{NL}} \simeq 3$ [18]. A crucial step in order to exploit all the information contained in the future *Planck* dataset is then to *extend the tools previously developed for temperature non-Gaussianity in order to include polarization*. This program has been recently started by the authors of [19], where the fast cubic statistic used to analyze WMAP temperature data [20, 21] was taken as a starting point to build an optimal cubic estimator that is sensitive to a combination of temperature and polarization primordial fluctuations. In this paper we will extend the non-Gaussian analysis toolkit in order to include the second fundamental element: Monte Carlo simulations of primordial non-Gaussian polarized CMB maps.

In section II we will summarize the original algorithm and describe its extension to polarization. We will then apply the fast cubic statistic of [19] to a set of polarized non-Gaussian maps. In this paper we will mainly focus our attention on map generation, so the purpose for applying the estimator is mainly to check the reliability of the final maps. This will be done by comparing the final outputs to theoretical predictions in ideal conditions. However in a forthcoming publication we will describe how we actually used the maps in order to test, calibrate and optimize the estimator.

II. GENERATION OF POLARIZED NON-GAUSSIAN CMB MAPS

Realistic simulations of non-Gaussian CMB maps are indispensable tools for measurements of non-Gaussian signals in the data, as they allow us to test and calibrate estimators and also to include and study all the spurious non-Gaussian signals introduced by contaminants like foregrounds, secondary anisotropies, instrumental noise and so on.

The first simulations of temperature maps with primordial non-Gaussianity from f_{NL} were carried out by Komatsu et al., and used extensively to study Gaussianity of the WMAP data [14] as well as non-trivial topology of the universe [22]. Then, Liguori et al. [23] have succeeded in increasing the computational speed, reducing the memory requirement and, most importantly, improving accuracy of the simulated temperature maps. We take this new algorithm developed in [23] as a starting point.

Our starting point is the relation between the primordial curvature perturbation Φ and the CMB multipoles $a_{\ell m}^X$ via radiation transfer functions Δ_{ℓ}^X .

$$a_{\ell m}^X = \int \frac{d^3k}{(2\pi)^3} \Phi(\mathbf{k}) Y_{\ell m}(\hat{k}) \Delta_{\ell}^X(k), \quad (3)$$

where X refers to either the temperature component T or the polarization component E.

The kind of non-Gaussianity we are considering has a very simple form in real space, where it is local and the non-Gaussian part of the curvature perturbation is simply the square of the Gaussian part (see formula 2). For this reason it is convenient to work in real space and define the real space transfer functions $\Delta_{\ell}(r)$ as:

$$\Delta_{\ell}^X(r) \equiv \frac{2}{\pi} \int dk k^2 j_{\ell}(kr) \Delta_{\ell}^X(k), \quad (4)$$

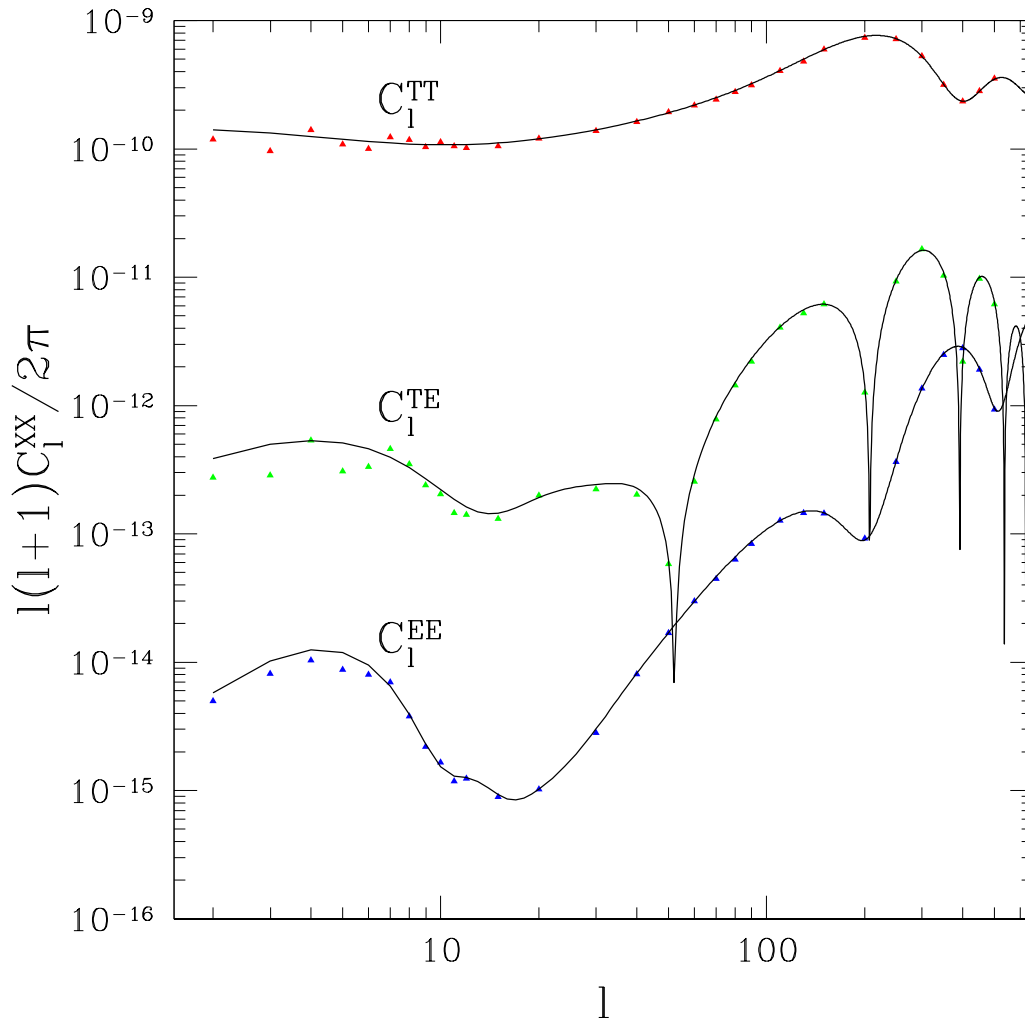


FIG. 1: CMB angular power spectra extracted from 10 simulations (triangles) are compared to the theoretical ones computed with CMBfast for the same model (solid black lines). The cosmological parameters are $\Omega_b = 0.042$, $\Omega_{cdm} = 0.239$, $\Omega_L = 0.719$, $h = 0.73$ $n = 1$, and $\tau = 0.09$ (same for all the following figures, unless otherwise stated).

where $j_\ell(kr)$ is the spherical Bessel function of order ℓ . It can be shown that $\Delta_\ell(r)$ links the primordial curvature perturbation $\Phi(\mathbf{r})$ in real space to the $a_{\ell m}^X$ through the following relation [14, 23]

$$a_{\ell m}^X = \int dr r^2 \Delta_\ell^X(r) \Phi_{\ell m}(r). \quad (5)$$

In this last formula we have introduced the quantities $\Phi_{\ell m}(r)$, which represent the spherical harmonic expansion multipoles of the curvature perturbation $\Phi(r, \hat{r})$ on a shell of given radius r . In formulae:

$$\Phi_{\ell m}(r) = \int d\Omega_{\hat{r}} Y_{\ell m}(\hat{r}) \Phi(r, \hat{r}). \quad (6)$$

We define the radius r as $r = c(\tau_0 - \tau)$, where c is the speed of light and $\tau_0 - \tau$ is the lookback conformal time. The radius r varies from the origin $r = 0$ to the present time cosmic horizon $r = c\tau_0$. The radii in which $\Phi_{\ell m}(r)$ must be generated depend on the features of the real space transfer function $\Delta_\ell^X(r)$ in equation (5). We will come back to this shortly.

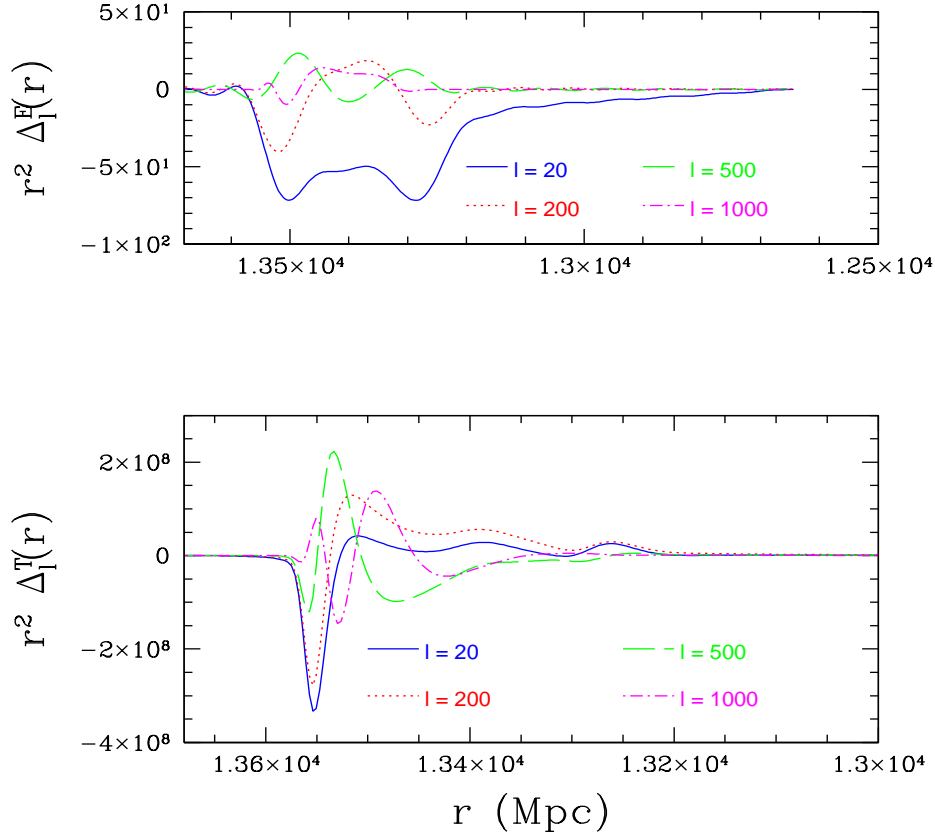


FIG. 2: Temperature (bottom panel) and polarization (upper panel) transfer functions at high ℓ at last scattering.

Let us assume for the moment that we have been able to numerically generate the Gaussian part of the curvature perturbation multipoles $\Phi_{\ell m}^L(r)$ for the chosen set of radii. Starting from here we can now generate the non-Gaussian part $\Phi_{\ell m}^{NL}(r)$ in the following way. First of all we harmonic transform $\Phi_{\ell m}^L(r)$ to get the gaussian part of the curvature perturbation in real space:

$$\Phi_L(r, \hat{r}) = \sum_{\ell} \sum_m \Phi_{\ell m}^L(r) Y_{\ell m}(\hat{r}). \quad (7)$$

Then we square $\Phi_L(r, \hat{r})$ to get the non Gaussian part of the curvature perturbation on each sampled spherical shell: $\Phi_{NL}(r, \hat{r}) \equiv \Phi_L^2(r, \hat{r}) - \langle \Phi_L^2(r, \hat{r}) \rangle$. We then calculate the multipoles of this non-Gaussian part through a backward harmonic transform:

$$\Phi_{\ell m}^{NL}(r) \equiv \int d\Omega_{\hat{r}} \Phi_{NL}(r, \hat{r}) Y_{\ell m}(\hat{r}). \quad (8)$$

Having computed $\Phi_{\ell m}^L(r)$ and $\Phi_{\ell m}^{NL}(r)$ we can finally obtain the Gaussian and non-Gaussian part of the CMB multipoles, $a_{\ell m}^{X,L}$ and $a_{\ell m}^{X,NL}$ respectively, by applying formula (5):

$$a_{\ell m}^{X,L} = \int dr r^2 \Delta_{\ell}^X(r) \Phi_{\ell m}^L(r) \quad (9)$$

$$a_{\ell m}^{X,NL} = \int dr r^2 \Delta_{\ell}^X(r) \Phi_{\ell m}^{NL}(r). \quad (10)$$

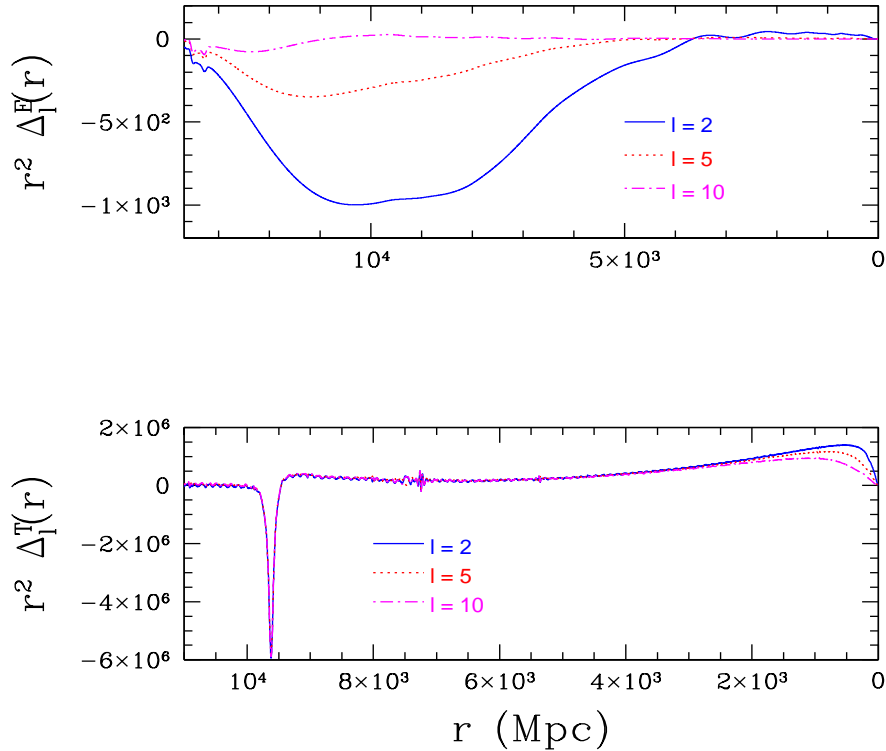


FIG. 3: Temperature (bottom panel) and polarization (upper panel) transfer functions at low ℓ (reionization and late ISW contributions are visible). The oscillations visible in the plots are little numerical artifacts which have negligible impact on the final results. We have explicitly checked this by increasing the resolution in the k and r -grid by factors of 2 and 4 without noticing any improvement in the accuracy of the final C_ℓ , that can be already reconstructed well using the sampling chosen in the paper (see fig. 1)

A CMB map for a chosen value of f_{NL} can then be obtained simply by summing $a_{\ell m}^{X,L} + f_{\text{NL}} a_{\ell m}^{X,NL}$. This means that with a single generation of $a_{\ell m}^X$ and $a_{\ell m}^{X,NL}$ it is possible to generate maps for any value of f_{NL} .

We are still left with one problem unsolved i.e. how do we generate the Gaussian curvature perturbation multipoles $\Phi_{\ell m}^L(r)$? This issue is complicated by the fact that curvature perturbation multipoles are correlated in real space. The obvious solution would be to generate curvature perturbations in Fourier space, $\Phi(\mathbf{k})$, Fourier transform back to real space to obtain $\Phi(\mathbf{x})$, change the coordinates from Cartesian to polar to obtain $\Phi(r, \hat{n})$, and finally harmonic transform to obtain $\Phi_{\ell m}(r)$. This is the original approach taken by [14], which is computationally quite expensive. Also, the coordinate transformation from Cartesian to polar limits accuracy of the maps, especially at high multipoles.

A novel approach developed in [23] solves this issue by generating $\Phi_{\ell m}(r)$ *directly*, without ever worrying about the coordinate transformation. It has been shown in [23] that the $\Phi_{\ell m}(k)$ and $\Phi_{\ell m}(r)$ are related by a spherical Bessel transform:

$$\Phi_{\ell m}(r) = \frac{(-i)^\ell}{2\pi} \int dk k^2 j_\ell(kr) \Phi_{\ell m}(k). \quad (11)$$

The problem with this expression is that the Bessel functions oscillate very rapidly. This implies that, for each (ℓ, r) , the integral above must be sampled in many different k in order to attain sufficient accuracy, thus making the computational cost of such an algorithm prohibitive. A much more convenient solution was found in [23]; the idea is to start with a set of Gaussian independent “white noise” coefficients $n_{\ell m}(r)$ characterized by the following correlation function:

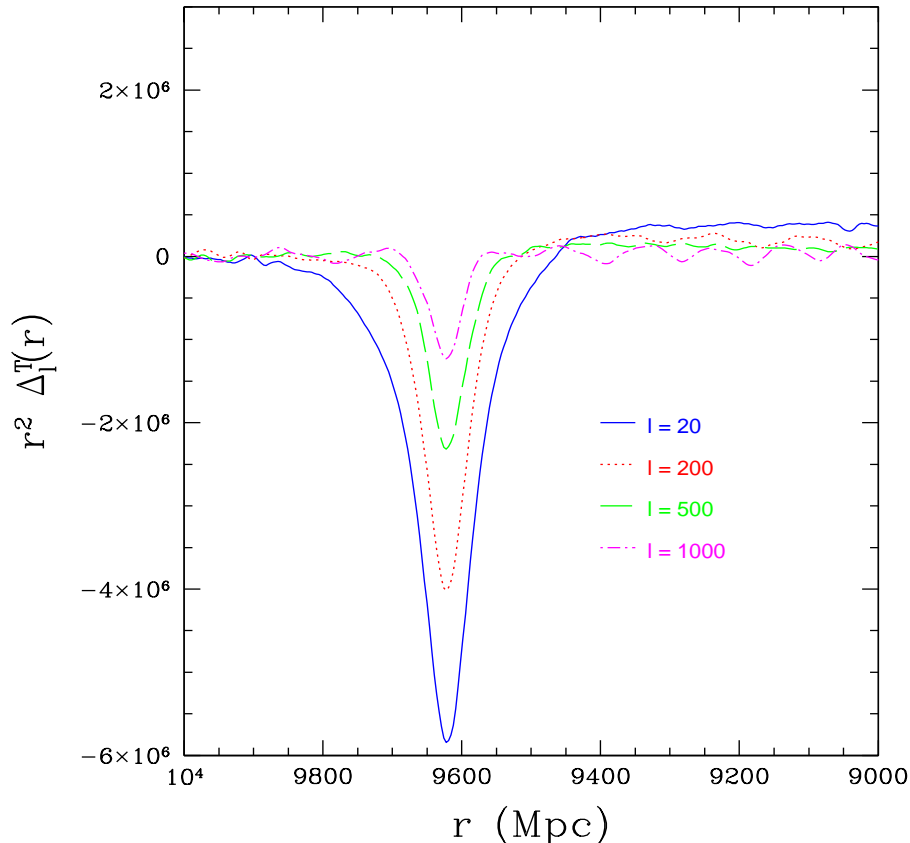


FIG. 4: Temperature transfer functions at high ℓ and r corresponding to the epoch of reionization. Polarization transfer functions at large ℓ are zero in this range.

$$\langle n_{\ell_1 m_1}(r_1) n_{\ell_2 m_2}^*(r_2) \rangle = \frac{\delta^D(r_1 - r_2)}{r^2} \delta_{\ell_1}^{\ell_2} \delta_{m_1}^{m_2} ; \quad (12)$$

it can be now shown that Gaussian curvature perturbation multipoles $\Phi_{\ell m}^L(r)$ with the right correlation properties can be obtained through a convolution of the $n_{\ell m}$ coefficients with suitable “filters” W_ℓ :

$$\Phi_{\ell m}^L(r) = \int dr_1 r_1^2 n_{\ell m}(r_1) W_\ell(r, r_1) , \quad (13)$$

where the functions W_ℓ are defined as

$$W_\ell(r, r_1) = \frac{2}{\pi} \int dk k^2 \sqrt{P_\Phi(k)} j_\ell(kr) j_\ell(kr_1) , \quad (14)$$

and $P_\Phi(k)$ is the power spectrum of the primordial curvature perturbation $\Phi_L(\mathbf{k})$. As depicted in Fig. 6, 7 the filter functions W_ℓ are smooth. Moreover, as also suggested by the Limber approximation applied to equation (14), $W_\ell(r, r_1)$ is narrowly peaked around r when $l \gtrsim 10$. This allows to sample the integral (13) in much less points than it would be required for the Bessel transform (11), thus making the problem computationally feasible. Obviously the problem of sampling a highly oscillatory integrand has not disappeared completely, but it has been reduced to the generation of $W_\ell(r, r_1)$. A trick here is that the filters $W_\ell(r, r_1)$ can be *pre-computed and stored* once and for all for a given cosmological model and their calculation does not enter in the actual Monte Carlo simulation algorithm. The same argument applies to the radiation transfer functions $\Delta_\ell(r)$ defined in (4).

Region	Bounds	Δr	N. of shells
Recombination	12632 Mpc $< r <$ 13682 Mpc	3.5 Mpc	300
Reionization 1	10007 Mpc $< r <$ 12632 Mpc	105Mpc	25
Reionization 2	9377 Mpc $< r <$ 10007 Mpc	35Mpc	18
Low redshifts	0 Mpc $< r <$ 9377 Mpc	105Mpc	89

TABLE I: Sampling of the r -coordinate in different regions of the simulation box. Different intervals must be sampled with different resolutions, according to the radiative transfer physics described in section II A.

Non-Gaussian temperature maps produced with the algorithms described in this section had been already described in [23]. Adding polarization to those maps is conceptually straightforward: all one needs to do is to replace $X = T$ with $X = E$ in the previous expressions. This amounts to generating the primordial curvature perturbation in exactly the same way for temperature and polarization maps and finally to use polarization transfer functions in place of temperature transfer functions in the line of sight integral (5) in order to get $a_{\ell m}^E$. Despite its conceptual immediateness, including polarization in the maps is not technically straightforward. The reason is that CMB polarization is produced by different physical mechanisms with respect to those producing CMB temperature anisotropies. The polarization transfer functions $\Delta_\ell^E(r)$ present then several differences with respect to $\Delta_\ell^T(r)$ and must be sampled in a different way, thus changing sampling regions and discretization of the r -coordinate which appears in $\Phi_{\ell m}(r)$, $\Delta_\ell(r)$, $W_\ell(r, r_1)$. These technical details will be illustrated in the following two sections.

A. Real space transfer functions

The cosmological model we chose to generate our non-Gaussian maps is characterized by the following parameters: $\Omega_{cdm} = 0.239$, $\Omega_b = 0.042$, $\Omega_\Lambda = 0.719$, $\tau = 0.09$, $h = 0.73$. We considered both a scale invariant primordial spectral index $n = 1$ and $n = 0.95$, the latest one being the WMAP 3-years best-fit value [15]. Starting from these parameters we generate and extract the Fourier space radiation transfer functions $\Delta_\ell^X(k)$ from a Boltzmann integrator, like for example CMBfast, and then make the integral (4) to get $\Delta_\ell^X(r)$. The behavior of $\Delta_\ell^X(r)$ reflects the underlying temperature and polarization CMB physics. In Fig. 2, we plot the real space temperature and polarization transfer functions for several different values of $\ell > 20$. For the model under examination the conformal time at last scattering, defined as the peak of the visibility function, is $\tau_* \simeq 277$ Mpc ($c = 1$) while the present cosmic horizon is $\tau_0 \simeq 13682$ Mpc. We thus expect most of the signal to be generated at $r_* \equiv \tau_0 - \tau_* \simeq 13400$ Mpc, consistently with what shown in the figure. Despite being smaller, contributions at lower redshifts cannot be neglected. We know that both reionization and the late integrated Sachs Wolfe effect produce significant contributions, especially at low ℓ 's. The reionization signal is particularly important for polarization, as it produces the observed bump at low ℓ 's in the polarization spectrum. This is reflected in the behavior of the temperature and polarization transfer functions at low ℓ in the post-recombination region, accordingly to what depicted in Fig. 4 and Fig. 3. According to the radiative transfer physics contained in $\Delta_\ell(r)$, the last scattering surface must be sampled using a large number of points in order to accurately reproduce the acoustic oscillations in the CMB spectrum, while in the low redshift region a good accuracy can be reached with a coarser sampling. More details about the sampled regions and intervals are in table I; the idea was to refine the r -grid until a good accuracy in the final C_ℓ from the simulated map was reached (see Fig. 1). However further sampling optimization in order to improve the speed of the algorithm is probably possible; an algorithm aimed at this kind of optimization is described in [24] in the context of bispectrum estimation.

B. Filter functions

After generating the real radiation transfer functions and fixing the radial coordinate grid, the $W_\ell(r, r_1)$ functions defined in (14) must be generated for each value of ℓ , r . Due to the highly oscillatory nature of the Bessel functions appearing in the definition of $W_\ell(r, r_1)$, a large number of points is required when sampling the integrand. This makes the numerical computation of $W_\ell(r, r_1)$ quite slow. However, as we were already stressing above, this is not a problem as the $W_\ell(r, r_1)$ functions are pre-computed and stored before the actual Monte Carlo map generation. When computing W_ℓ it is useful to make the simple substitution $t = kr$ in the integrand of (14). This substitution yields:

$$W_\ell(r, r_1) = 2\pi r^{\frac{-n-2}{2}} I_\ell\left(\frac{r_1}{r}\right), \quad (15)$$

where we have defined:

$$I_\ell(x) \equiv \int dt t^{\frac{n}{2}} j_\ell(t) j_\ell(tx). \quad (16)$$

From the last formulae we see that $W_\ell(r, r_1)$ actually depends only on the ratio r_1/r and not on r_1 and r separately. This allows to reduce the dimensionality of the problem and thus to speed up the calculations.

In figures 6 and 7 we plot some W_ℓ functions for different values of ℓ , r , r_1 . As expected, $W_\ell(r, r_1)$ approximates a Dirac delta function centered on r with increasing accuracy for larger and larger ℓ . So for $l \gtrsim 10$ the coordinate r_1 needs to be sampled in a narrow region centered around r . On the other hand, for low values of ℓ , $W_\ell(r, r_1)$ is non-negligible over a broad r_1 range. Thus a coarser r_1 sampling over a larger r_1 interval is required in this case. To check the accuracy of the numerical computation of $W_\ell(r, r_1)$ it is useful to compute the angular power spectrum of $\Phi_{\ell m}^L(r)$ on a given spherical shell. Starting from formula (13), and using the correlation properties of the coefficients $n_{\ell m}(r_1)$ described by eqn. (12) one gets:

$$\begin{aligned} \langle \Phi_{\ell_1 m_1}^L(x) \Phi_{\ell_2 m_2}^{L*}(y) \rangle &= \frac{2}{\pi} \delta_{\ell_1 \ell_2} \delta_{m_1 m_2} \int dr_1 dr_2 r_1^2 r_2^2 [\langle n_{\ell_1 m_1}(r_1) n_{\ell_2 m_2}^*(r_2) \rangle \times \\ &\quad \times W_{\ell_1}(x, r_1) W_{\ell_2}(y, r_2)] \\ &= \frac{2}{\pi} \int dr_1 dr_2 r_1^2 r_2^2 \frac{\delta^{(D)}(r_1 - r_2)}{r_1^2} W_{\ell_1}(x, r_1) W_{\ell_2}(y, r_2) \\ &= \frac{2}{\pi} \delta_{\ell_1 \ell_2} \delta_{m_1 m_2} \int dr_1 r_1^2 W_{\ell_1}(x, r_1) W_{\ell_2}(y, r_2), \end{aligned} \quad (17)$$

which immediately yields:

$$\langle |\Phi_{\ell m}^L(r)|^2 \rangle = \frac{2}{\pi} \int dr_1 r_1^2 W_\ell^2(r, r_1). \quad (18)$$

Alternatively it is possible to use the following formula for the $\Phi_{\ell m}$ correlation function [23]:

$$\langle \Phi_{\ell_1 m_1}^L(x) \Phi_{\ell_2 m_2}^{L*}(y) \rangle = \frac{2}{\pi} \delta_{\ell_1 \ell_2} \delta_{m_1 m_2} \int dk k^2 P_\Phi(k) j_{\ell_1}(kx) j_{\ell_2}(ky), \quad (19)$$

to find:

$$\langle |\Phi_{\ell m}^L(r)|^2 \rangle = \frac{2}{\pi} \int dk k^2 P(k) j_\ell^2(kr). \quad (20)$$

For a primordial curvature perturbation power spectrum described by a power law expression, $P(k) = Ak^{n-4}$, and using a well-known formula for the Sachs-Wolfe effect, one finally gets:

$$\langle |\Phi_{\ell m}^L(r)|^2 \rangle = \frac{2^{n-3} A r^{1-n}}{\pi} \frac{\Gamma(\ell + \frac{n}{2} - \frac{1}{2}) \Gamma(3-n)}{\Gamma(\ell + \frac{5}{2} - \frac{n}{2}) \Gamma^2(2 - \frac{n}{2})}. \quad (21)$$

For a scale invariant primordial power spectrum one obtains, as expected, $|\langle \Phi_{\ell m}^L(r)|^2 \rangle \propto 1/l(l+1)$. As we were anticipating above, one can use formulae (18) and (21) to test the $\Phi_{\ell m}(r)$ power spectrum on different shells and the normalization of $W_\ell(r, r_1)$. Results from our simulations are shown in picture 5.

Noise	Sky-cut	$\langle f_{\text{NL}} \rangle$	σ_{maps}	σ_{fisher}
No	No	102.5	11.1	6.9
Homogeneous	No	104.5	15.8	11
Homogeneous	$f_{\text{sky}} = 80$	105.2	25.7	12.2

TABLE II: Results obtained from the application of the fast temperature + polarization cubic statistics of [19] to a set of 300 non-Gaussian maps with an input f_{NL} of 100. First column describes the noise properties of the map, second column is the adopted sky-cut, third column is the average f_{NL} measured by the estimators, fourth column is the measured f_{NL} standard deviation, fifth column is the expected standard deviation from a Fisher matrix analysis (i.e. neglecting corrections from the non-Gaussian part of the multipoles).

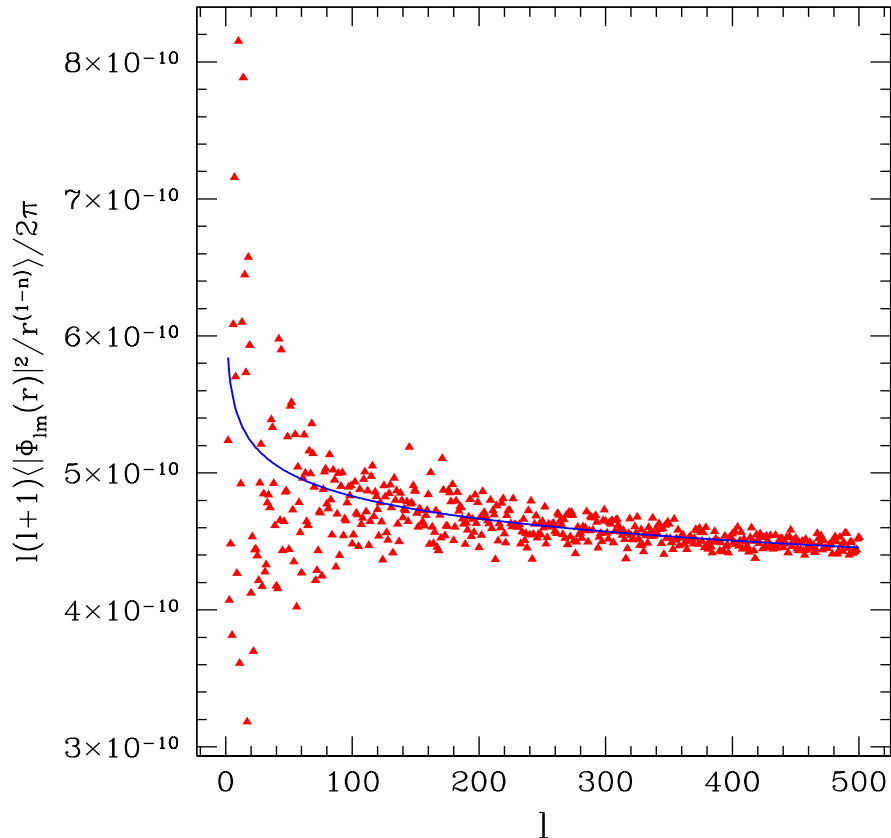


FIG. 5: Angular power spectrum of the Gaussian curvature perturbation multipoles $\Phi_{\ell m}^L(r)$ obtained by averaging over all the spherical shells of a given simulation. In this example we consider a spectral index $n = 0.95$ and divide $|\Phi_{\ell m}^L(r)|$ by $\sqrt{r^{(1-n)}}$ in order to make the normalization of the spectrum independent of the shell radius before averaging. We compare the results extracted from our simulations (red triangles) to the expected shell power spectrum obtained from formula (21), (blue line)

III. FAST CUBIC STATISTICS AND NON-GAUSSIAN MAPS

In order to test our algorithm we applied the temperature + polarization fast-cubic statistics described in [19] to a set of 300 non-Gaussian simulations obtained from the cosmological parameters $\Omega_b = 0.042$, $\Omega_{\text{cdm}} = 0.239$, $\Omega_L = 0.719$, $h = 0.73$, $n = 1$, $\tau = 0.09$. In figure 8 we show a temperature and a polarization intensity map extracted from this set.

When sky-cut is included a non-trivial correlation between large and small ℓ is introduced. This correlation in turn produces a leakage of power from high to low multipoles which tends to bias the estimator. This effect has been accurately studied in [19], where it has also been shown that removing the lowest multipoles from the analysis allows

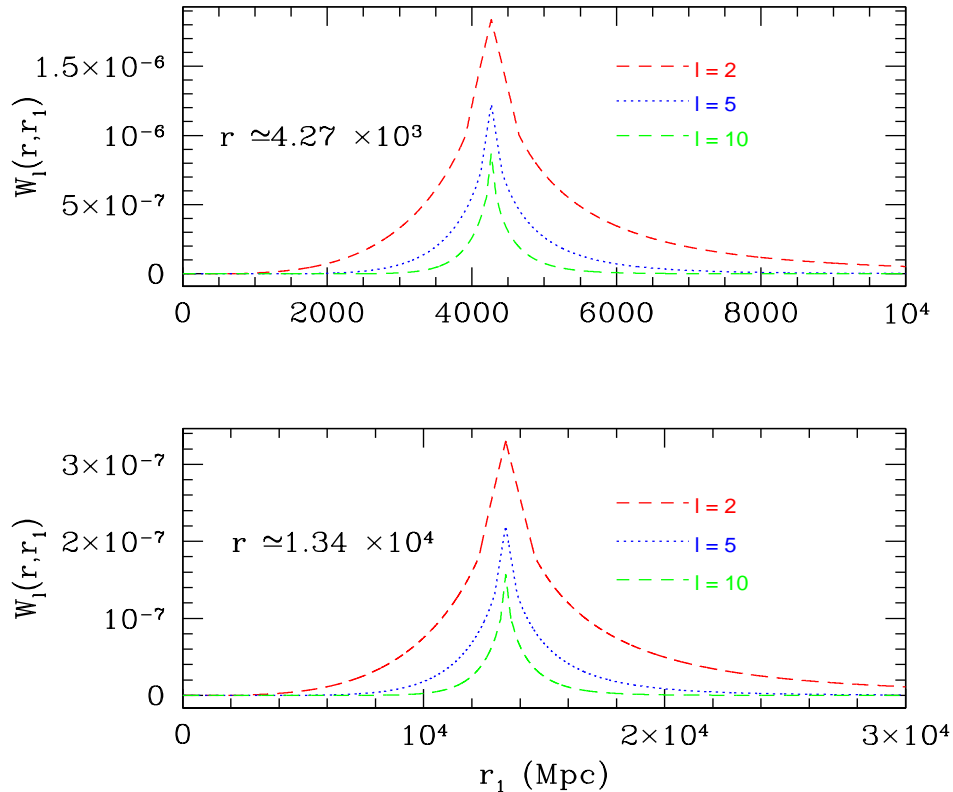


FIG. 6: Filter functions $W_\ell(r, r_1)$ plotted as a function of r_1 for two different fixed values of r . Here we consider low l -values $l \leq 10$, for which the $W_\ell(r, r_1)$ are different from zero and must therefore be sampled in a large r_1 region. At high l these functions become more and more peaked around r , as shown in Fig. 7.

to circumvent this problem without a significant loss of signal. For this reason the first 30 multipoles were not used in our analysis when a skycut was considered. The exact ℓ_{min} was determined by preliminary applying the estimator to a set of Gaussian simulation and estimating its variance as a function of ℓ_{min} . We considered different sky cut levels and accounted for the presence of homogeneous noise. Our results are summarized in table II .

Our computation provides evidence for the unbiasedness of the estimator but shows at the same time a discrepancy between the calculated error bars and Fisher matrix based expectations (note that these expectations are obtained at zeroth order in f_{NL} , thus neglecting f_{NL} -dependent terms in the three point function). These discrepancies are f_{NL} dependent: for small undetectable f_{NL} we find a good agreement between Fisher matrix estimates and our results whereas increasing values of f_{NL} produce larger and larger differences. This effect had been predicted and explained by the authors of [16]. It arises from f_{NL} dependent correction terms in the variance of the estimator. These terms become important when f_{NL} is detected at several sigma. The comparison of our results with those in [16] is necessarily approximate because the latter were obtained in the flat-sky approximation and ignoring radiation transfer functions. However we can still cross-check for a qualitative agreement between the two results. Using the above approximations, the f_{NL} -dependent formula describing the estimator variance is:

$$\sigma^2 = \langle \sigma^2 \rangle_{f_{NL}=0} \left(1 + \frac{8f_{NL}^2 A N_{pix}}{\pi \ln N_{pix}} \right), \quad (22)$$

where $\langle \sigma^2 \rangle_{f_{NL}=0}$ is the estimator variance in the Gaussian case (i.e. the variance estimated from the Fisher matrix), A is the amplitude of primordial perturbations and N_{pix} is the number of pixels in the map. To simplify the notation we define $\sigma_0^2 \equiv \langle \sigma^2 \rangle_{f_{NL}=0}$. Following [16] we consider an f_{NL} detection at $n\sigma_0$. From the formula above:

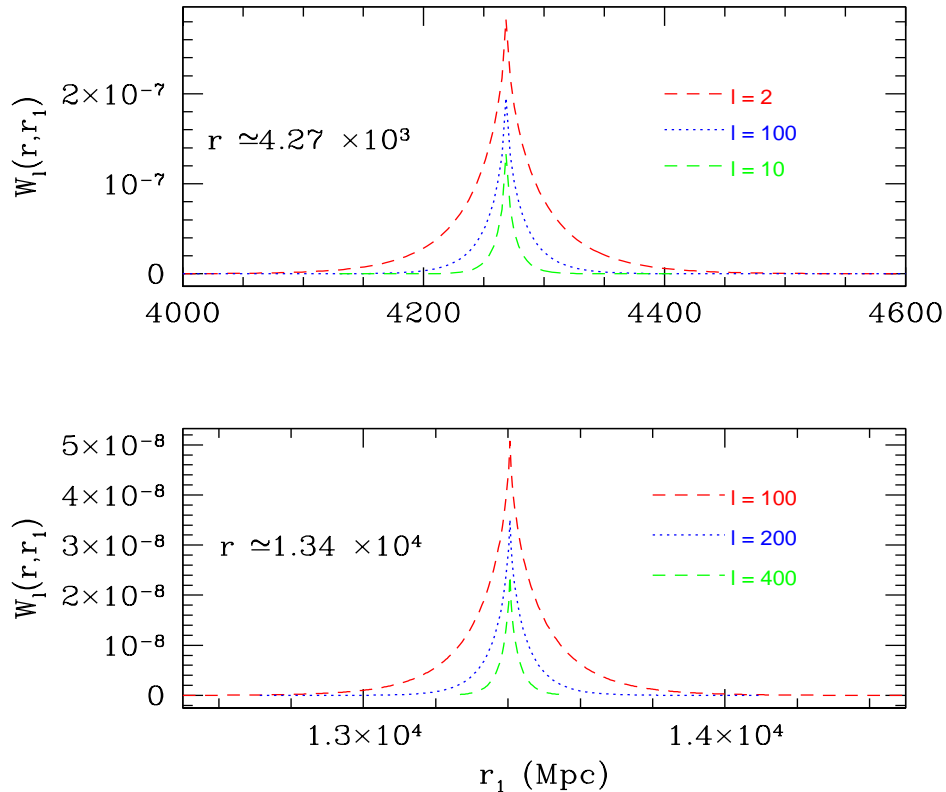


FIG. 7: Filter functions $W_\ell(r, r_1)$ plotted as a function of r_1 for two different fixed values of r . As ℓ gets larger, the $W_\ell(r, r_1)$ becomes more and more narrowly peaked around r .

$$\sigma^2 = \sigma_0^2 + \frac{2n^2\sigma_0^2}{\pi \ln^2 N_{pix}} . \quad (23)$$

We then find the expected relative correction to the variance as:

$$\frac{\langle \sigma^2 \rangle}{\sigma_0^2} - 1 = \frac{2n^2}{\pi \ln^2 N_{pix}} . \quad (24)$$

In our analysis we have $N_{pix} = 3145728$ (HEALPix $n_{side} = 512$) and $\sigma_0 = 6.9$ for the case without sky-cut or noise (see second line of table II). We have an input f_{NL} of 100, so this corresponds to $n = 14.5$. Plugging this numbers into the equation above we obtain a relative correction of 0.6 which is about one third of the observed $\sigma^2/\sigma_0^2 - 1 = 1.6$ but in qualitative agreement considering the approximations contained in eqn. (24). For large enough f_{NL} eqn. (24) also predicts the variance of the estimator to decrease as $1/\ln^2 N_{pix} \sim 1/\ln \ell_{max}$, much slower than the Fisher matrix forecast of $\sigma \sim 1/\ell_{max}$. We explicitly tested this prediction on sets of simulated maps with different $f_{NL}, N_{pix}, \ell_{max}$ and we found a good agreement between theory and simulations, as depicted in figure 9. Thus the results obtained analytically in [16] under several simplified assumptions are confirmed by our numerical approach, which works in full-sky and includes radiation transfer functions.

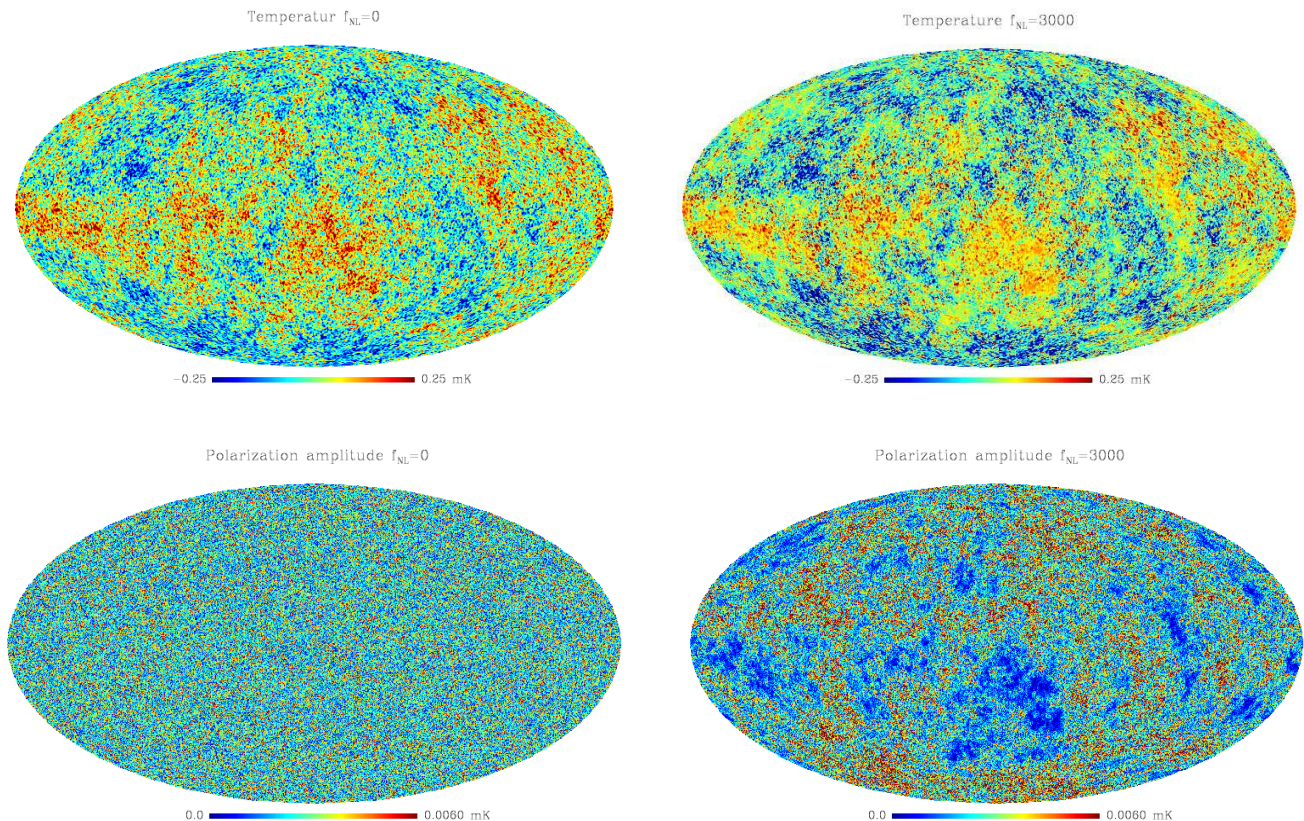


FIG. 8: Left column: temperature and polarization intensity Gaussian CMB simulations obtained from our algorithm. Polarization intensity is defined as $I \equiv \sqrt{Q^2 + U^2}$ where Q and U are the Stokes parameters. Right column: temperature and polarization non-Gaussian maps with the same Gaussian seed as in the left column and $f_{\text{NL}} = 3000$. The reason for the choice of such a large f_{NL} is that we wanted to make non-Gaussian effects visible by eye in the figures. The cosmological model adopted for this plots is characterized by: $\Omega_b = 0.042$, $\Omega_{\text{cdm}} = 0.239$, $\Omega_L = 0.719$, $h = 0.73$, $n = 1$, $\tau = 0.09$. Temperatures are in mK .

IV. COMPUTATIONAL REQUIREMENTS AND POSSIBLE APPLICATIONS

Our algorithm takes about 3 hours on a normal PC to generate a map with $\ell_{\text{max}} = 500$, $N_{\text{pix}} \simeq 10^6$, corresponding to an analysis at WMAP angular resolution. The most time consuming part is the computation of the harmonic transforms required to generate $\Phi_{\ell m}^{\text{NL}}$ from $\Phi_{\ell m}^{\text{L}}$. As we generate the primordial curvature perturbation in about 400 spherical shells we need to make 400 calls to the HEALpix synfast and anafast subroutines respectively. Thus we can roughly quantify the CPU time for a non-Gaussian simulation at a given resolution as the time required to produce 800 Gaussian maps at the same resolution. It is thus clear that the generation of maps at the resolution achieved by *Planck* constitutes a very intensive computational task and requires a parallelization of the algorithm. Only the temperature version of the code has been parallelized so far, enabling us to generate a map at $\ell_{\text{max}} = 3000$, $n_{\text{side}} = 2048$ in about 2 hours on 60 processors. A set of 300 temperature maps with this angular resolution has been generated and tested. Extending the parallel code in order to include polarization should be straightforward, because all the sampling-related problems have been already solved for the serial version of the algorithm presented in this paper and including polarization transfer functions is trivial. The total CPU time to generate a map is going to be unchanged with respect to the temperature-only version, because the primordial curvature perturbation generation scheme is identical and the total number of shells is basically the same. We would like to note here that a different algorithm has been proposed for the generation of non-Gaussian maps in [24]. This algorithm can generate maps with a given two and three point function but does not reproduce the higher order correlation functions predicted by the model. By making this approximation, the authors of [24] are able to dramatically speed up the computation (~ 3 minutes for a map at $\ell_{\text{max}} = 1000$ on a single processor). In the limit of weak non-Gaussianity neglecting higher order correlation functions should be a good approximation. In particular it has been explicitly shown in [16] that no

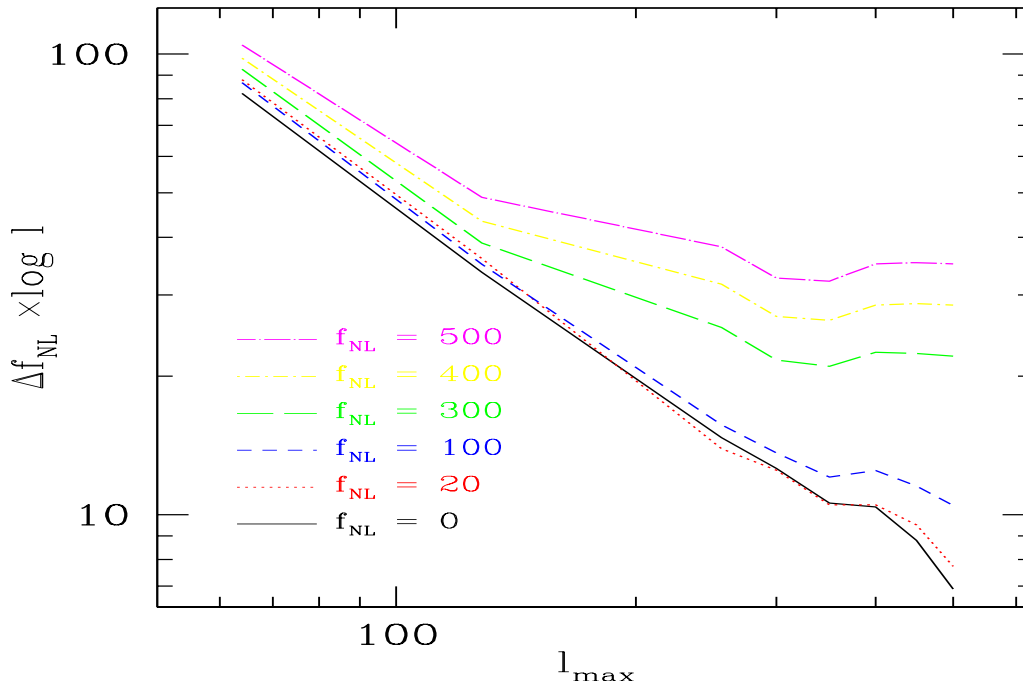


FIG. 9: Error bars estimated from different sets of simulations including various ℓ_{max} and input f_{NL} . The error bars are compared to the corresponding Fisher matrix forecast. As explained in the text, an f_{NL} -dependent correction to the estimator variance make the error bars to scale as $1/\ln \ell_{max}$ instead of $1/\ell_{max}$ when f_{NL} is large enough to produce a several sigma detection at a given angular resolution.

additional information on f_{NL} can be added by applying estimators based on higher order correlators. This conclusion is strictly related to the presence of f_{NL} -dependent correction terms in the variance of the local bispectrum. Note however that these terms have originally been studied in flat-sky approximation and neglecting transfer functions. As an application of our algorithm, in the previous section of this paper we have explicitly cross-checked the results of [16] using our simulations which are full-sky and account for radiative transfer [31]

We would also like to stress that being able to correctly reproduce higher order correlation functions in the simulations was fundamental in order to make this test. The reason is that what we are studying here is actually an f_{NL} -dependent correction to the 6-point function (bispectrum variance) coming from a product of the 2-point function with the 4-point function (see again [16] for further details).

Another obvious application for these simulated maps is given by the possibility to use them in order to test and calibrate not only the bispectrum but any kind of estimator (like e.g. Minkowski functionals, wavelets and so on). In particular the analytical formulae of the Minkowski functionals recently derived by [25] may be compared with our simulations of the temperature maps. Our preliminary investigation shows a very good agreement, which gives us further confidence in the accuracy of the simulated temperature maps. Despite the optimality of the bispectrum just discussed above, using different estimators is still important, especially in view of a possible f_{NL} detection by Planck. Alternative estimators should in fact be used in this case in order to cross-validate such detection.

Furthermore, it is interesting to notice that the algorithm we are describing is not only able to generate non-Gaussian CMB maps, but it also produces maps of the primordial curvature perturbation $\Phi(r, \hat{r})$, sampled in the relevant radii for the generation of the final CMB signal. This allows us to apply and test tomographic reconstruction techniques of the curvature perturbation like those proposed in [26]. This will be the object of a forthcoming publication [27]. Finally we would like to observe that the same elegant r -sampling optimization technique introduced in [24] can be implemented in our case in order to drastically reduce the number of radii in which the primordial curvature perturbation must be evaluated. Following the results of [24], a good accuracy in the final maps should be obtained using only 20 spherical shells in our code after this optimization. As we are now using 400 shells, we estimate a speed improvement of a factor ~ 20 . In this way the parallel version of the algorithm should allow the generation of a map at full Planck resolution in ~ 10 minutes against the present 2 hours. For this reason CPU time does not seem to be a problem and tests of non-Gaussianity at *Planck* angular resolution using our algorithm are perfectly feasible.

V. CONCLUSIONS

In this paper the algorithm for the generation of non-Gaussian primordial CMB maps originally introduced in [23] has been generalized by including a polarization component in the simulations. Using this generalized algorithm we have produced a set of 300 temperature and polarization maps at WMAP angular resolution. We have then analyzed these simulations using the fast cubic temperature + polarization statistics recently introduced by the authors of [19]. We have verified that we can extract the correct input f_{NL} from the maps, thus checking at the same time both the unbiasedness of the estimator and the reliability of the simulations. We also studied the estimator variance on different sets of maps including various angular resolutions and input f_{NL} . We found that an f_{NL} -dependent correction to the estimator variance induces a discrepancy between the error bars extracted from the simulations and the Fisher matrix estimate of the same error bars at $f_{\text{NL}} = 0$. We therefore confirmed previous findings by the authors [16]. At the same time, differently from previous approaches, our numerical Monte Carlo analysis allowed us to work in full sky and account for radiation transfer functions. We finally discussed future applications of our simulations, which will include a detailed analysis of non-Gaussian temperature and polarization simulations at Planck angular resolution.

Acknowledgments

We acknowledge the use of the HEALpix software [28, 29] (see <http://healpix.jpl.nasa.gov/> for further information on HEALpix). We acknowledge partial financial support from from the ASI contract Planck LFI Activity of Phase E2. We would like to thank Paolo Cabella for stimulating discussions and contributions in an early phase of this project. We would also like to thank Paolo Creminelli for useful discussions. ML is supported by PPARC.

-
- [1] V. Acquaviva, N. Bartolo, S. Matarrese and A. Riotto, Nucl. Phys. B 667 (2003) 119, [arXiv:astro-ph/0209156]
 - [2] J. Maldacena, JHEP 0305 (2003) 013, [arXiv:astro-ph/0210603]
 - [3] D.H. Lyth, C. Ungarelli, D. Wands, Phys.Rev. D67 (2003) 023503, [arXiv:astro-ph/0208055]
 - [4] N. Bartolo, S. Matarrese, A. Riotto, JHEP 0404 (2004) 006, [arXiv:astro-ph/0308088]
 - [5] N. Bartolo, E. Komatsu, S. Matarrese, A. Riotto, Phys.Rept. 402 (2004) 103-266, [arXiv:astro-ph/0406398]
 - [6] N. Arkani-Hamed, P. Creminelli, S. Mukohyama, M. Zaldarriaga, JCAP 0404 (2004) 001, [arXiv:hep-ph/0312100]
 - [7] M. Alishahiha, E. Silverstein, D. Tong Phys.Rev. D70 (2004) 123505, [arXiv:hep-th/0404084]
 - [8] X. Chen, Phys.Rev. D72 (2005) 123518, [arXiv:astro-ph/0507053]
 - [9] G.I. Rigopoulos, E.P.S. Shellard, B.J.W. van Tent, [arXiv:astro-ph/0511041]
 - [10] L.E. Allen, S. Gupta, D. Wands, JCAP 0601 (2006) 006, [arXiv:astro-ph/0509719]
 - [11] E. Sefusatti and E. Komatsu, [arXiv:0705.0343]
 - [12] A. Pillepich, C. Porciani, S. Matarrese, Astrophys.J. 662, 1 (2007) 1-14, [arXiv:astro-ph/0611126]
 - [13] A. Cooray, Phys.Rev.Lett. 97 (2006) 261301, [arXiv:astro-ph/0610257]
 - [14] E. Komatsu, et al., Astrophys.J.Suppl. 143 (2003) 119
 - [15] D.N. Spergel, et al., Astrophys.J.Suppl. 170 (2007) 377
 - [16] P. Creminelli, L. Senatore, M. Zaldarriaga, JCAP 0703 (2007) 005, [arXiv:astro-ph/0606001]
 - [17] E. Komatsu and D. Spergel, Phys.Rev. D63 (2001) 063002, [arXiv:astro-ph/0005036]
 - [18] D. Babich, M. Zaldarriaga, Phys.Rev. D70 (2004) 083005, [arXiv:astro-ph/0408455]
 - [19] A. P. S. Yadav, E. Komatsu, B. D. Wandelt, arXiv:astro-ph/0701921
 - [20] E. Komatsu, B. Wandelt, D. Spergel, Astrophys.J. 634 (2005) 14-19, [arXiv:astro-ph/0305189]
 - [21] P. Creminelli, A. Nicolis, L. Senatore, M. Tegmark, M. Zaldarriaga, JCAP 0605 (2006) 004
 - [22] N.J. Cornish, D.N. Spergel, G.D. Starkman, E. Komatsu, Phys.Rev.Lett. 92 (2004) 201302
 - [23] M. Liguori, S. Matarrese, L. Moscardini, Astrophys.J. 597 (2003) 57-65, [arXiv:astro-ph/0306248]
 - [24] K. M. Smith, M. Zaldarriaga, [arXiv:astro-ph/0612571]
 - [25] C. Hikage, E. Komatsu, T. Matsubara, Astrophys. J., 653 (2006) 11
 - [26] A. P. S. Yadav, B. D. Wandelt, Phys.Rev. D71 (2005) 123004, [arXiv:astro-ph/0505386]
 - [27] A. P. S. Yadav *et al.*, in preparation
 - [28] K.M. Gorski, et al., Astrophys.J. 622 (2005) 759-771, [arXiv:astro-ph/0409513]
 - [29] K.M. Gorski, et al., [arXiv:astro-ph/9905275]
 - [30] This limit is verified in our case as non-Gaussianity from inflation is small.
 - [31] As a subject of future work, all these checks will be repeated by taking into account possible contaminant effects, like e.g. foreground residuals, second order anisotropies, systematics, map-making effects and so on, in order to study their impact on the estimator.